MDPI

Article

Bismuth Nano-Rods Wrapped with Graphene and N-Doped C as Anode Materials for Potassium- and Sodium-Ion Batteries

Shuangyan Qiao [1,2], Yongning Liu [3,*], Kai Wang [1,2,*] and Shaokun Chong [1,2,*]

[1] Research & Development Institute, Northwestern Polytechnical University in Shenzhen, Shenzhen 518063, China; iamsyqiao@nwpu.edu.cn
[2] Frontiers Science Center for Flexible Electronics, Xi'an Institute of Flexible Electronics, Xi'an Institute of Biomedical Materials & Engineering, Northwestern Polytechnical University, Xi'an 710072, China
[3] State Key Laboratory for Mechanical Behavior of Materials, School of Material Science and Engineering, Xi'an Jiaotong University, Xi'an 710049, China
* Correspondence: ynliu@mail.xjtu.edu.cn (Y.L.); iamkwang@nwpu.edu.cn (K.W.); iamskchong@nwpu.edu.cn (S.C.)

Abstract: Alloying-type anode materials have considerably promoted the development of potassium-ion batteries (PIBs) and sodium-ion batteries (SIBs), enabling them to achieve high-energy-density. However, large volume expansion and sluggish dynamic behavior have become key issues affecting electrochemical performance. Herein, bismuth (Bi) nano-rods are anchored on reduced graphene (rGO) and encapsulated via N-doped C (NC) to construct Bi@rGO@NC architecture as anode materials for SIBs and PIBs. The hierarchical confinement effect of three-dimensional conductive networks can not only improve electrode stability upon cycling via suppressing the large volume variation, but also eliminate the band gap of Bi and accelerate ion diffusion, thereby exhibiting favorable electrochemical reaction kinetics. Thus, Bi@rGO@NC contributes an ultra-long lifetime, over 1000 cycles, and an outstanding rate property to SIBs and PIBs. This work can pave the way for the construction of high-performance alloying-type anode materials for SIBs and PIBs.

Keywords: potassium-ion batteries; sodium-ion batteries; anode materials; bismuth; composites

1. Introduction

Lithium-ion batteries (LIBs) have been widely applied in the fields of portable electronic devices, electric vehicles, and large-scale electric energy storage (EES) systems, with the remarkable advantages of higher energy density and longer cycle life. In this context, the limited lithium resources in the Earth's crust and their uneven distribution make it difficult to meet the demand for both electric vehicles and grid-scale energy storage, which has gradually aroused concern. There is an urgent need for low-cost, resource friendly, high-energy-density alternative batteries to satisfy the rapidly increasing need [1–3]. Potassium ion batteries (PIBs) and sodium ion batteries (SIBs) provide potential solutions because of the relatively abundant reserves (2.09 wt.% for K and 2.36 wt.% for Na vs. 0.0017 wt.% for Li) and low cost, and similar storage mechanisms to LIBs [4]. Low redox potential, close to lithium's (-2.93 V vs. K$^+$/K, -2.71 V vs. Na$^+$/Na, -3.04 V vs. Li$^+$/Li), allows PIBs and SIBs to achieve high energy density. Because of the weaker Lewis acidity, smaller Stokes' radius, and higher mobility of K$^+$ and Na$^+$ in electrolyte, SIBs and PIBs can achieve better electrochemical kinetic behavior than LIBs [5–7]. However, the issue with PIBs and SIBs lies in the large ion radius (1.38 Å of K$^+$, 0.98 Å of Na$^+$), which would easily disrupt the electrode materials, leading to sluggish dynamic and poor cyclability [8,9].

Significant progress has been made in the research of electrode materials for PIBS and SIBs over the past years. In particular, the structure–property relationship, ion storage mechanism, and optimization strategy of different cathode materials (represented by

layered oxides, polyanion compounds, Prussian blue analogs, and organic materials) have been thoroughly explored, and achieved encouraging performance results [10–14]. As for layered oxides (A_xMO_2, A = Na and K, M = transition metal), studies mainly focus on O3- and P2-type structures (alkaline metal ions coordinated in the octahedral and prismatic sites, respectively), where O3-type oxides can contribute to high theoretical specific capacity due to high content alkaline metal ions, while P2-type oxides can boost excellent rate capability, benefitting the large channels for ion migration [15,16]. Polyanionic compounds (fluorophosphates, pyrophosphates, etc.) can exhibit high working voltage and superior cyclic stability owing to the stable crystal structure [17]. Prussian blue analogues ($A_xM[Fe(CN)_6]_y \cdot zH_2O$, where A represents alkali ions, and M stands for transition metals) show great promise because their open framework structure and large interstitial sites can accommodate reversible de/intercalation of Na-/K-ion, thus guaranteeing high specific capacity, good rate properties, and a long lifetime [18]. Organic cathode materials possess flexible frameworks and large primary interlayer spacing, and are suitable as host materials with a high capacity [19].

In contrast, there is still a shortage of suitable anode materials to match these mature cathode materials. Among the emerging anode materials, carbonaceous materials (such as hard carbon, soft carbon, graphene, etc.) provide excellent chemical stability, but their low capacity cannot be ignored [20]. Although organic compounds possess controllable structures and high electrochemical performance due to multi-electron reversible redox reaction, their low electronic/ionic conductivity and high solubility are serious obstacles [21]. Generally, conversion-type anode materials (transition-metal oxide, chalcogenides, nitride, phosphide, etc.) deliver high theoretical specific capacity, yet high redox potential and huge volume change reduce the long cycles of the electrode [22]. Thus, low working voltage coupled with high theoretical capacity thrust alloy-based electrode materials (Sn-based, Sb-based, Bi-based, P-based, and so on) to the forefront [23]. As an alloy-based anode material, bismuth (Bi) has attracted increasing interest from researchers, thanks to its nontoxic nature, large interlayer spacing, excellent electrical conductivity (7.8×105 S·m^{-1}), high volumetric capacity (3750 mAh·cm^{-3}), and suitable reaction potential [24,25]. Nevertheless, the large volume expansion ($\approx$244% for Na_3Bi, $\approx$411% for K_3Bi) caused by alloying processes and poor kinetic behavior have become the key scientific challenges given their adverse impact on Na/K-ion storage properties [26–28]. These issues could be properly addressed by the strategies of nano-structuring, engineering morphology, and composite constructure with C-based materials [29–34]. The Bi nanoparticles wrapped in graphene to form a Bi@graphene nanocomposite delivered a high capacity of 561 mAh g^{-1} for SIBs; however, the cycle life requires improvement [35]. Later, Zhang et al. improved the cycle life of Bi@graphene to 200 cycles via optimizing the electrolyte with a more stable solid electrolyte interphase layer [36]. In spite of these advances, there are still huge challenges in achieving high capacity during long cycling ranges with stable structures.

Herein, Bi nano-rods encapsulated by reduced graphene oxide and nitrogen-doped carbon (Bi@rGO@NC), constructed through solvothermal and calcination processes, serve as alloying anode materials for PIBs and SIBs. The electronic structure of Bi is adjusted through the synergistic effect of NC and rGO, and thus exhibits conductor behavior. In addition, the hierarchical encapsulation effects of NC and rGO can assist in a high electron/ion transport ability, and relieve the huge lattice stress generated by volume expansion, thereby improving electrochemical dynamic processes and achieving excellent electrode stability upon cycling. Hence, Bi@rGO@NC electrodes deliver superior rate capability and cyclic stability over 1000 cycles in PIBs and SIBs.

2. Materials and Methods

2.1. Materials Synthesis

A total of 4 mmol of thioacetamide (TAA) was dissolved in a mixture of ethanol (15 mL, >99.7%) and glycerol (5 mL, 99%). Then, 2 mmol $BiCl_3$ and a certain amount of graphene oxide was added under magnetic stirring to form a homogeneous solution, which was

heated at 180 °C for 12 h in a Teflon-lined stainless-steel autoclave. A Bi_2S_3@rGO sample was collected using freeze-drying after washing with ethanol and water several times.

Then, 121 mg of trihydroxy methyl aminomethane was dissolved in 100 mL of deionized water and 15 µL of HCl (36~38%) under stirring to form a homogeneous solution. Subsequently, 200 mg of dopamine hydrochloride and 200 mg of Bi_2S_3@rGO were added with ultrasonic and stirring, and stirred for 24 h at room temperature. Finally, Bi@rGO@NC composite was acquired through annealing at 500 °C for 3 h in an Ar atmosphere.

2.2. Materials Characterizations

An X-ray Diffraction (XRD, D8 Advance, Bruker, Karlsruhe, Germany) with Cu Kα radiation (λ = 1.5406 Å) was employed to examine the crystal structure of the synthesized material. The microscopic morphology of the sample was observed using field-emission scanning electron microscopy (FESEM, ZEISS-300, ZEISS, Oberkochen, Germany). An energy dispersion spectrum (EDS) mapping was also performed during SEM observation. The Raman spectrum was recorded using a WITec-Alpha300R spectrometer with a laser excited at 532 nm. Thermogravimetric analysis (TGA, TG 209 F3, NETZSCH, Freistaat Bayern, Germany) was carried out in air atmosphere at a heating rate of 10 °C/min from room temperature to 800 °C to evaluate the carbon content and Bi loading of materials. The surface chemical composition and electronic state of the sample were obtained via X-ray photoelectron spectroscopy (XPS, Shimadzu Kratos Axis Supra, Al Ka radiation, Shimadzu Kratos, Manchester, UK). The pore size distribution and the Brunauer–Emmett–Teller (BET) specific surface area were measured using N_2 adsorption/desorption method on a BELSORP-MAX tester.

2.3. Electrochemical Tests

The working electrodes were prepared by mixing active material with acetylene black and polyvinylidene difluoride (PVDF), in a weight ratio of 8:1:1, in 1-Methyl-2-pyrrolidinone (NMP), which was coated onto Cu foil and dried at 80 °C for 12 h. The electrode was cut into discs with a diameter of 12 mm, and the mass loading of active material in each electrode was controlled at the range of 1.5–2.0 mg. Coin-type cells (CR-2025) were assembled in a glove box ($H_2O \leq 0.01$ ppm, $O_2 \leq 0.01$ ppm) for the electrochemical measurement, where K/Na metal (Aladdin) and glass microfiber were used as counter electrode and separator, respectively. Then, 1 M $NaClO_4$ in a mixture of EC and DEC (volume ratio of 1:1) with 5% fluoroethylene carbonate (FEC) was employed as the electrolyte for SIBs. A total of 1 M KPF_6 in ethylene carbonate (EC), diethyl carbonate (DEC), propylene carbonate (PC), with a volume ratio of 1:1:1, was utilized as the electrolyte for PIBs. Galvanostatic charge/discharge tests were performed on a Neware battery test system at a voltage range of 0.01~3.0 V. Cyclic voltammetry (CV) was determined on a CHI 660E electrochemical workstation. A Galvanostatic intermittent titration technique (GITT) test was applied via charging/discharging at 50 mA·g^{-1} for 600 s and then relaxation for 3600 s at open circuit voltage.

2.4. Computational Methods

Theoretical calculations based on density functional theory (DFT) methods were performed in the CASTEP package. For electron exchange–correlation, the Perdew–Burke–Ernzerhof generalized gradient approximation (GGA-PBE) was used. The energy cutoff of plane wave basis was set to 500 eV, which was adequate to achieve energy convergence. The super cell of $3 \times 3 \times 1$ was used to calculate the adsorption energy of K/Na ions to avoid the interaction energy between ions and obtain more accurate results. The K-ion adsorption energy was obtained by the formula of $E_{ads.} = E_{Bi-K} - E_{Bi} - E_K$.

3. Results and Discussion

3.1. Morphology and Structure Analysis

The Rietveld refinement X-ray Diffraction (XRD) pattern of Bi@rGO@NC composite is displayed in Figure 1a. It can be indexed as a rhombohedral Bi structure with the space group of R-3m (JCPDS NO. 85-1329), whose sharp diffraction peaks show good crystallinity with no impurities [37]. The detailed refinement parameters are listed in Table 1, whose unit cell parameters are determined as a = b = 4.56 Å and c = 11.90 Å, and the fitting results are satisfactory (R_{wp} = 5.76%, R_p = 4.43%). The crystal structure diagram of Bi is shown in Figure 1b, in which the inherent layered structure is accompanied by a large interlayer distance of 3.95 Å, which provides favorable conditions for the de/intercalation of sodium- and potassium-ions [38]. The field-emission scanning electron microscopy (FESEM) image of Bi@rGO@NC is displayed in Figure 1c. It can be observed that the Bi nanorods are tightly anchored on graphene substrate and wrapped with an N-doped C layer, and the diameter of Bi nanorods is about 10~20 nm. Energy-dispersive spectroscopy (EDS) mapping images are displayed in Figure 1d to further illustrate the elemental composition. It can be clearly observed that Bi, C, and N elements are distributed uniformly throughout the Bi@rGO@NC architecture. Such a hierarchical structure can provide a buffer area to accommodate the large volume expansion of Bi electrodes during alkaline-ion insertion and extraction, and the nanorod morphology of Bi can shorten the ion transport paths to enhance the rate capability. In Raman spectra (Figure 1e), two distinct characteristic bands at ~1350 and ~1580 cm^{-1} are related to D-band (sp^3 hybridized disordered carbon) and G-band (sp^2 hybridized graphitic carbon), respectively [8]. The intensity ratio of D-band and G-band (I_D/I_G) is 1.09, implying a high amorphous degree of carbon in Bi@rGO@NC, which could offer better electron conductivity and is conducive to improving electrochemical kinetic behavior. Moreover, two peaks can be observed at ~2685 and ~2930 cm^{-1}, which correspond to the characteristic 2D band and D+G band of rGO, respectively, confirming the successful introduction of rGO [39]. The N_2 adsorption/desorption profile in Figure 1f exhibits type-IV isotherm with H3 hysteresis loops, revealing a hierarchically porous structure, which contributes to the rapid Na- and K-ion diffusion capability. It is also confirmed by the pore size distribution curve (inset of Figure 1f, pore size of <10 nm). Furthermore, Bi@rGO@NC possesses a high specific surface area of 70.87 $m^2 \cdot g^{-1}$, which offers efficient buffering space for volume change during alloying/de-alloying processes. As shown in the TGA curve (Figure 1g), the final weight percentage of Bi_2O_3 was 44.69%, and the mass loss after 200 °C is ascribed to the oxidation from Bi to Bi_2O_3 and the consumption of carbon in the air. The loading of Bi in Bi@rGO@NC can be calculated to be 40.08% using the equation Bi wt.% = 100 × (4 × M_{Bi} × weight percentage of Bi_2O_3)/(2 × M_{Bi2O3}) [40,41].

Table 1. Lattice parameters of Bi@rGO@NC obtained by Rietveld refinement XRD.

a = b = 4.56128, c = 11.90056, α = β = 90°, γ = 120°			
	X	Y	Z	Occupation
Bi	0.66667 (0)	0.33333 (0)	0.56724 (0)	1
R_p = 4.43%, R_{wp} = 5.76%			

X-ray photoelectron spectroscopy (XPS) was performed to investigate the surface composition and electronic state of elements in Bi@rGO@NC. The survey spectrum in Figure S1a indicates the existence of Bi, C, N, and O elements. In Bi 4f fitting spectra (Figure 1h), two peaks located at 164.6 and 159.4 eV can be assigned to Bi $4f_{5/2}$ and Bi $4f_{7/2}$ of Bi-Bi bonds, demonstrating that Bi exists in metal form [42]. The high-resolution C 1s spectrum (Figure 1i) can be fitted into three peaks, at 284.7, 285.7, and 289.1 eV, which belong to C-C/C=C, C-O/C-N, and O-C=O, respectively [43]. The O 1s spectrum (Figure S1b) is divided into three peaks, corresponding to C-O (533.5 eV), C-OH (532.2 eV), and C=O (530.8 eV), respectively [44]. Figure 1j presents N 1s spectra, where the peaks at 400.3 and 398.5 eV are related to pyrrolic N and pyridinic N [45], respectively, which is evidence of

successful N doping into the carbon layer. It is well known that the introduction of N can increase defects in carbon layers, which is conducive to improved electronic conductivity and surface wettability, and thus leads to rapid ion storage dynamic process and good electrolyte wetting [46].
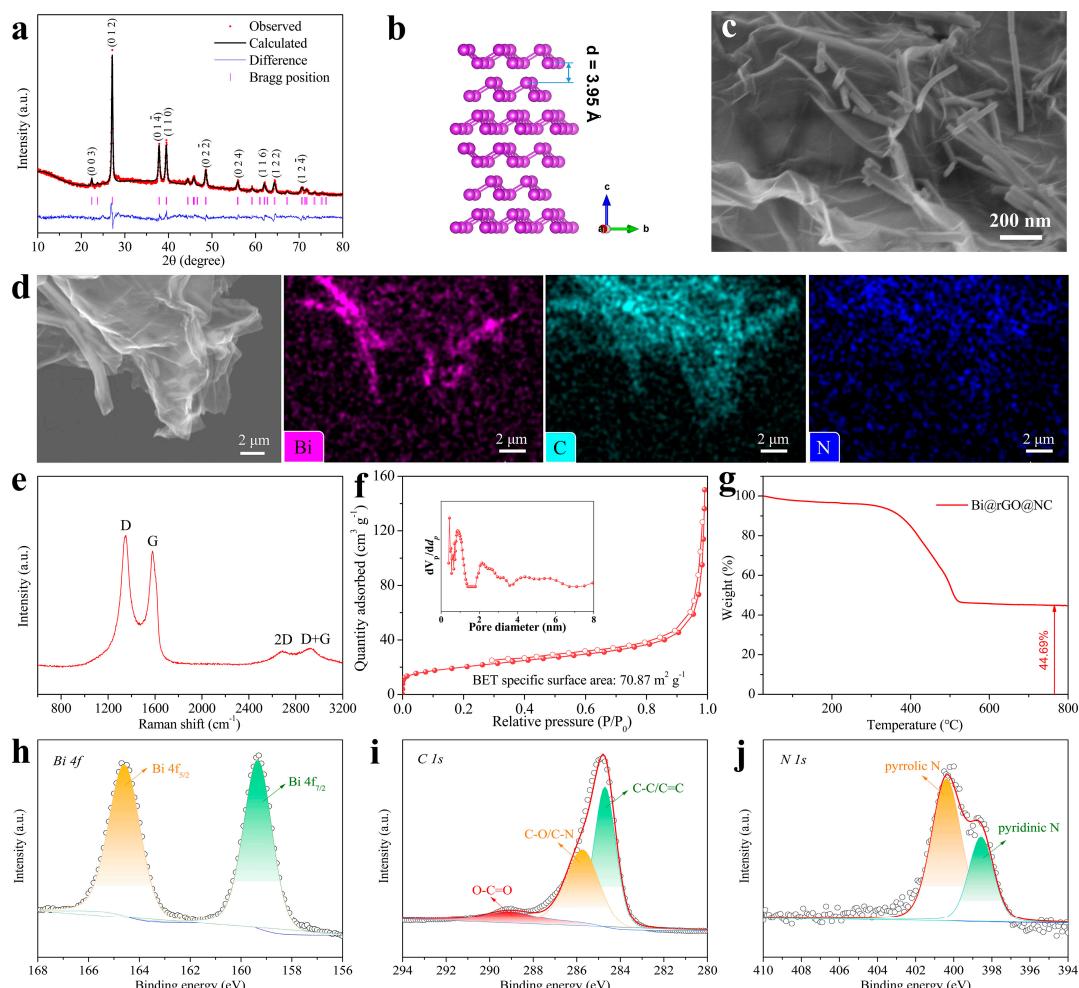

Figure 1. Structural and morphological characterization: (**a**) Rietveld refinement XRD pattern of Bi@rGO@NC; (**b**) crystal structure diagram of Bi; (**c**) FESEM image; (**d**) EDS mapping images of Bi@rGO@NC; (**e**) Raman spectrum; (**f**) N_2 adsorption-desorption isotherm and pore size distribution (inset); (**g**) TGA curve; (**h**) high resolution Bi 4f; (**i**) C 1s; and (**j**) N 1s spectra of Bi@rGO@NC.

3.2. Electrochemical Performances

In SIBs, cyclic voltammetry (CV) was conducted in the potential window of 0.01–3.0 V to investigate the redox behavior of Bi@rGO@NC. Figure 2a gives CV curves of the initial third cycles at 0.1 mV s^{-1} in SIBs, where a peak at 1.05 V can be judged as the formation of a solid–electrolyte interface (SEI) during the first cathodic process. In the first sodiation process, two peaks can be observed, at 0.50 and 0.24 V. These are attributed to the two-step alloying reactions of Bi → NaBi → Na$_3$Bi [47]. The anodic sharp peaks around 0.75 and 0.86 V are ascribed to the dealloying process of Na$_3$Bi to form Bi. As a result of the activation process of the electrode, the reduction peaks of subsequent cycles slightly move to higher voltage, while the oxidation peaks show no obvious shift, indicating outstanding electrochemical reversibility and small polarization of the alloying-dealloying process between Bi and Na$_3$Bi [31]. Figure 2b depicts the galvanostatic charge/discharge curves of Bi@rGO@NC at 50 mA·g^{-1} for SIBs, contributing high initial charge/discharge

capacities of 285.5/501.5 mAh·g^{-1}. Such large irreversible specific capacity originates from the formation of SEI film and the decomposition of electrolytes.
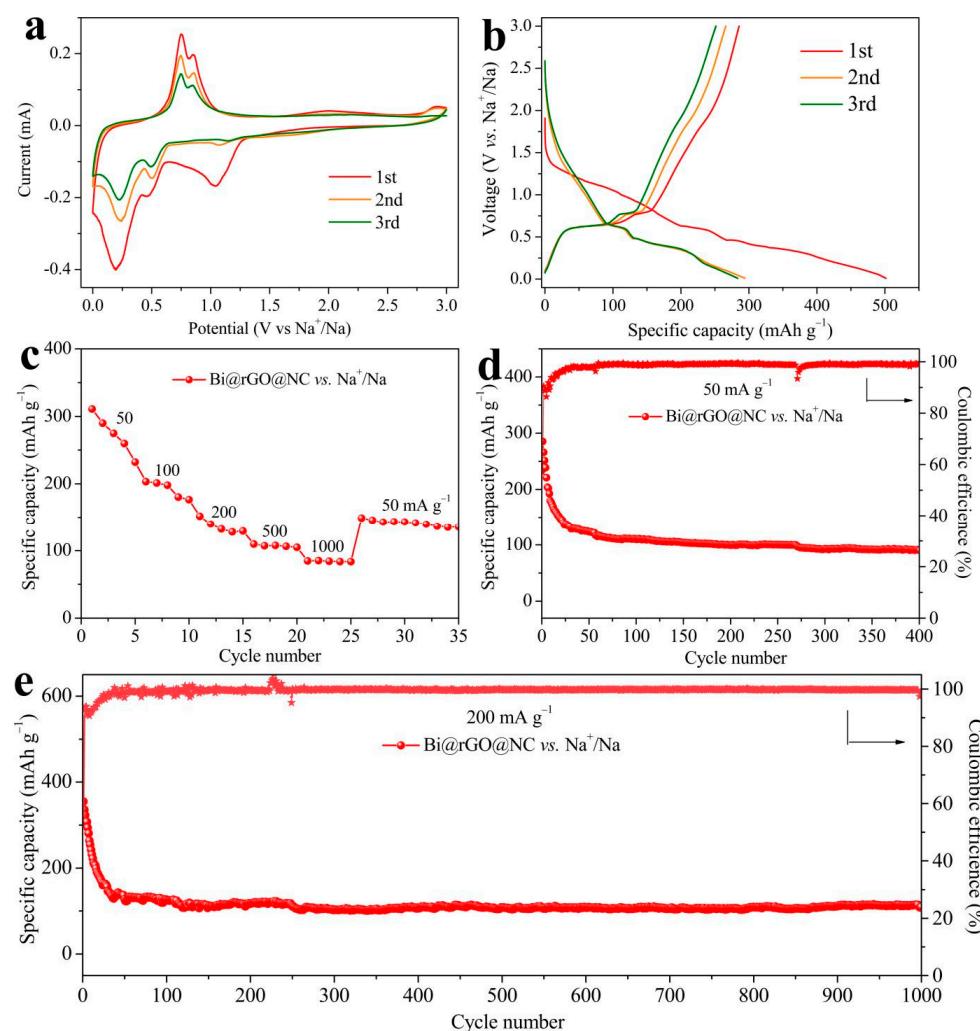

Figure 2. Electrochemical performances of Bi@rGO@NC for SIBs: (**a**) CV curves at 0.1 mV·s^{-1} and (**b**) discharge/charge profiles of the first three cycles at 50 mA·g^{-1}; (**c**) rate capability; (**d**) cycle performance at 50 mA·g^{-1}; and (**e**) at 200 mA·g^{-1}.

Rate capability analysis was performed to understand the fast and stable redox kinetics. The finding was that Bi@rGO@NC electrodes in SIBs provide reversible specific capacities of 203.4, 151.7, 109.6, and 84.5 mAh·g^{-1} at 100, 200, 500, and 1000 mA·g^{-1} (Figure 2c), respectively. When the current density returns to 50 mA·g^{-1}, the reversible capacities of 149.0 mAh·g^{-1} for SIBs can be obtained. Figure 2d displays the cyclic property at 50 mA·g^{-1}, showing great cycling stability over 400 cycles for SIBs, with a high Coulombic efficiency of around 99% after several initial cycles, where Bi@rGO@NC maintains high-capacity retention value of 90.5 mAh·g^{-1} after 400 cycles. Long-term cycling performance of Bi@rGO@NC electrodes was further evaluated at 200 mA·g^{-1} (Figure 2e). Superior cyclability for Na-ion storage can be achieved for Bi@rGO@NC, showing ultra-long lifetime over 1000 cycles with the capacity retention of 109.7 mAh·g^{-1}, and a capacity decay rate of only 0.069% per cycle. The good electrochemical performance of Bi@rGO@NC architecture may be derived from the synergistic effects of the N-doped carbon layer and graphene. Figure S3 displays the cycling performances of electrode materials with and without N-doped carbon to illustrate its effect on cycling stability. Obviously, Bi@rGO@NC consistently exhibits much better cycling stability with than without N-doped C electrode at 50 and

200 mA·g^{-1}, demonstrating that N-doped C can effectively enhance electrode stability via accommodating the large volume expansion of Bi during cycling.

In PIBs, two pairs of oxidation/reduction peaks at 0.69/1.32 and 0.16/0.70 V (vs. K$^+$/K) in Figure 3a correspond to the two-step alloying/dealloying process between Bi and K. Overlapping CV profiles manifest highly reversible K-ion insertion/extraction behavior. There are two pairs of plateaus located at 0.74/1.29 and 0.19/0.66 V in Figure 3b, which are consistent with the CV result. For K-ion storage, Bi@rGO@NC delivers high first reversible specific capacity of 348.3 mAh·g^{-1}. Meanwhile, the charge specific capacities of 179.6, 156.6, 66.2, and 31.9 mAh·g^{-1} can be acquired at current densities of 100, 200, 500, and 1000 mA·g^{-1}, respectively (Figure 3c). When the current density turns back to 50 mA·g^{-1}, the reversible specific capacity of 176.4 mAh·g^{-1} can be obtained. By comparison, it can be observed that superior rate capability can be achieved for SIBs compared with PIBs, demonstrating better electrochemical kinetics for reversible Na-ion storage. Figure 3d shows the cycling performance of Bi@rGO@NC at 50 mA·g^{-1}, showing that it maintains a specific capacity of 52.1 mAh·g^{-1} after 400 cycles. Furthermore, the Columbic efficiency of the cell increases continuously upon cycling, eventually reaching around 99%, suggesting great electrochemical reversibility. The long-term cycling property was further measured at 200 mA·g^{-1}, as displayed in Figure 3e, exhibiting a long lifespan over 1000 cycles, while the capacity retention is slightly lower than that in SIBs.
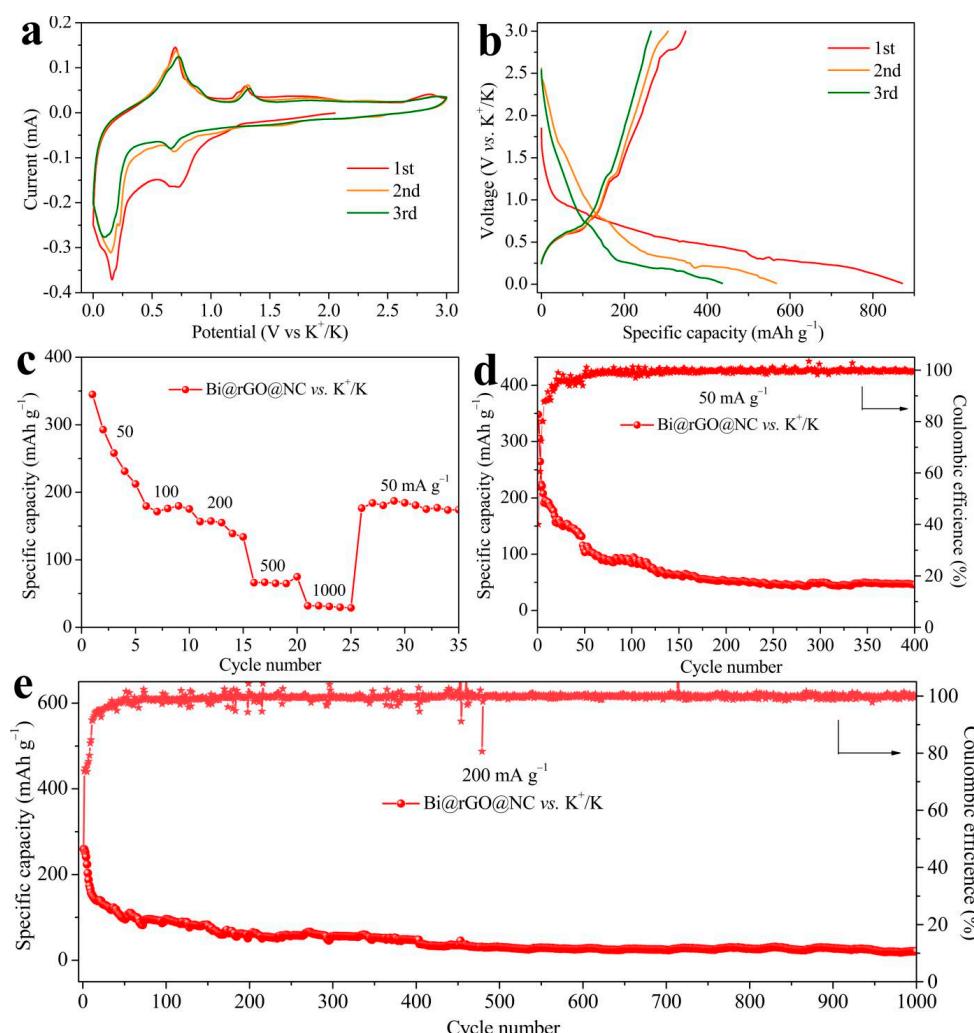

Figure 3. Electrochemical performances of Bi@rGO@NC for PIBs: (**a**) CV curves at 0.1 mV·s^{-1} and (**b**) discharge/charge profiles of the first three cycles at 50 mA·g^{-1}; (**c**) rate capability; (**d**) cycle performance at 50 mA·g^{-1} and (**e**) at 200 mA·g^{-1}.

All these results confirm that Bi@rGO@NC is a promising anode material for Na- and K-in storage. It is worth mentioning that the Bi@rGO@NC composite shows better cyclic stability and rate property in SIBs than PIBs because the larger ionic radius of K in PIBS adversely impacts the kinetic behavior and stability of the electrode material. Ex situ FESEM images of Bi@rGO@NC after 20 cycles for both SIBs and PIBs were collected to understand the electrode integrity. Although Bi@rGO@NC suffers from volume expansion to some degree, as shown in Figure S2a, its rod-like morphology is well maintained, indicating great morphology robustness during repeated sodiation/desodiation processes. By contrast, Bi@rGO@NC could not withstand the huge stress induced by de/intercalation of large-sized K-ion, leading to the formation of bulky agglomerates (Figure S2b), which results in relatively faster capacity decay.

3.3. Electrochemical Kinetics

Density functional theory (DFT) based on first principles calculations was employed to evaluate the kinetics of Bi@rGO@NC for Na-/K-ion storage at the atomic level. As evidenced by the electronic density of states (DOS, Figure 4a), Bi@rGO@NC exhibits metallic behavior. Such a result demonstrates that the introduction of a double carbon layer makes Bi change from a semiconductor to a conductor [48], thus effectively adjusting the electronic structure of Bi and improving its electronic conductivity, which provides favorable conditions for alkaline-ion storage. The band structures in Figure 4b also clearly evidence its metallicity. Furthermore, the calculated adsorption energy of K^+ and Na^+ on Bi@rGO@NC are −1.63 eV and −1.64 eV, respectively, based on the model of K/Na-embedded Bi@rGO@NC crystal (Figure 4c), indicating the favorable tendency of thermodynamic adsorption. Therefore, it is concluded that N-doped carbon and rGO matrices enhance the electronic conductivity and Na-/K-ion adsorption capacity of Bi.
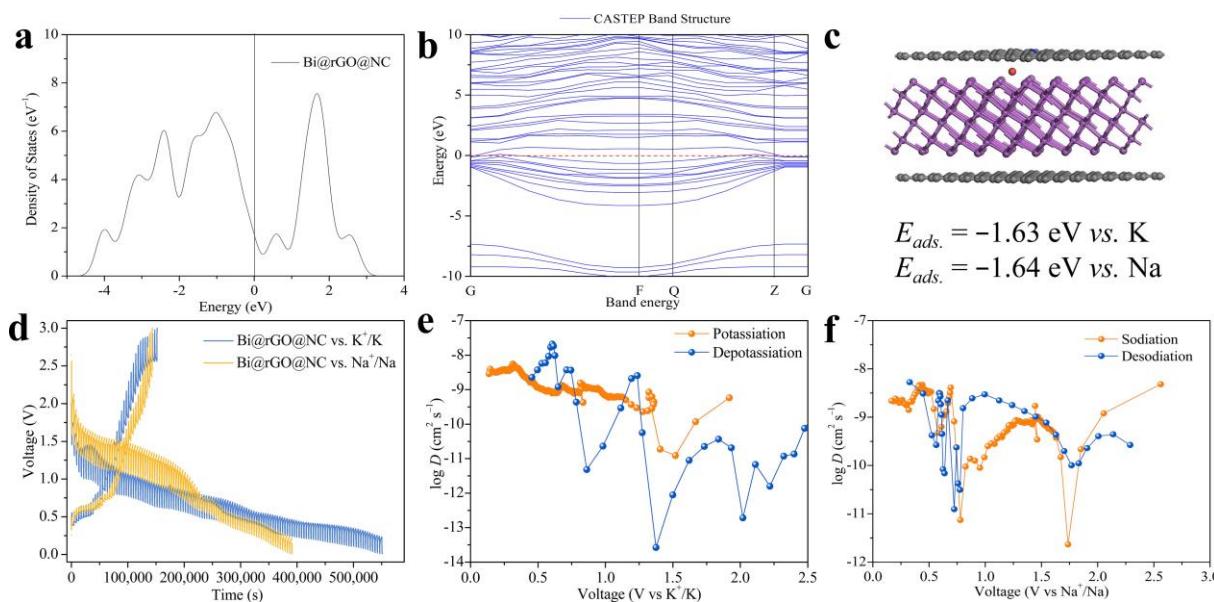

Figure 4. First-principle calculations and electrochemical kinetics: (**a**) DOS and (**b**) band structure; (**c**) structural model for calculation (K/Na atom in red, N atom in blue, C atom in black); (**d**) GITT curves; (**e**) the calculated D_{K+}; and (**f**) D_{Na+} plots of Bi@rGO@NC from GITT.

The ion transport dynamic behavior was analyzed using galvanostatic intermittent titration techniques (GITT) at 50 mA·g^{-1} (Figure 4d). Na-/K-ion diffusion coefficient (D_{Na+} and D_{K+}) was calculated based on the formula of $D_{Na+/K+} = 4/\pi\tau \, (n_m V M/S)^2 \cdot (\Delta E_s/\Delta E_\tau)^2$, where τ, n_m, V_m, S, ΔE_s and ΔE_τ can be ascribed to the time of the pulse, molar number of the active material, molar volume of electrode material, active surface area of electrode in contact with electrolyte, change in battery voltage during charging/discharging, and change in voltage in equilibrium state, respectively [49]. The calculated diffusion coeffi-

cients (D_{Na+} and D_{K+}) are in the range of $10^{-14} \sim 10^{-8}$ cm²·s⁻¹ for K-ion storage (Figure 4e) and $10^{-12} \sim 10^{-8}$ cm²·s⁻¹ for Na-ion storage (Figure 4f). Such results illustrate that hierarchical carbon encapsulation plays a key role in the electrochemical dynamics. The K-/Na-ion diffusion and capacitive behavior were evaluated by CV curves. Analogous shapes at different scanning rates (Figure 5a) suggest good response capability to high-rates for Na-ion storage. The proportion of capacitance at different scan rates can be quantified with the formula $I = k_1 v + k_2 v^{1/2}$, where $k_1 v$ and $k_2 v^{1/2}$ correspond to the contributions of capacitive and diffusion behavior, respectively [50]. The equation can be adjusted to $I/v^{1/2} = k_1 v_{1/2} + k_2$, where k_1 (slope) and k_2 (intercept) are obtained by linear fitting of $I/v^{1/2}$ *vs.* $v^{1/2}$. Finally, the capacitance and diffusion contributions can be determined by averaging the values of $k_1 v/(k_1 v + k_2 v^{1/2})$ and $k_2 v^{1/2}/k_1 v + k_2 v^{1/2}$) under each voltage. The diffusion-controlled ratio is 85.7% for SIBs at 0.1 mV·s⁻¹ (Figure 5b). As displayed in Figure 5c, the capacitance contributions at scanning rates of 0.2, 0.3, 0.5, 1.0, 2.0 and 3.0 mV s⁻¹ are calculated to be 18.09%, 20.65%, 24.26%, 29.8%, 36.01% and 36.9%, respectively. In terms of PIBs, the polarization is more severe at large sweep speeds, as shown in Figure 5d, which explains why rate performance of PIBs is worse than that of SIBs. In addition, K-ion diffusion contribution ratio is calculated to be 84.11% at 0.1 mV·s⁻¹ (Figure 5e), illustrating that the capacity is determined by diffusion behavior to a significant extent. Similarly, the proportion of capacitance shows an upward trend with the increase in sweep rates. The high proportion of capacitive behavior contributes to outstanding rate ability and cycling stability. Figure S4 shows the electrochemical impedance spectroscopy (EIS) plots of Bi@rGO@NC electrode after 10 cycles, where a much lower charge transfer resistance (R_{ct}) value can be achieved for SIBs compared with that for PIBs, demonstrating fast electron and Na-ion transfer dynamic behavior.
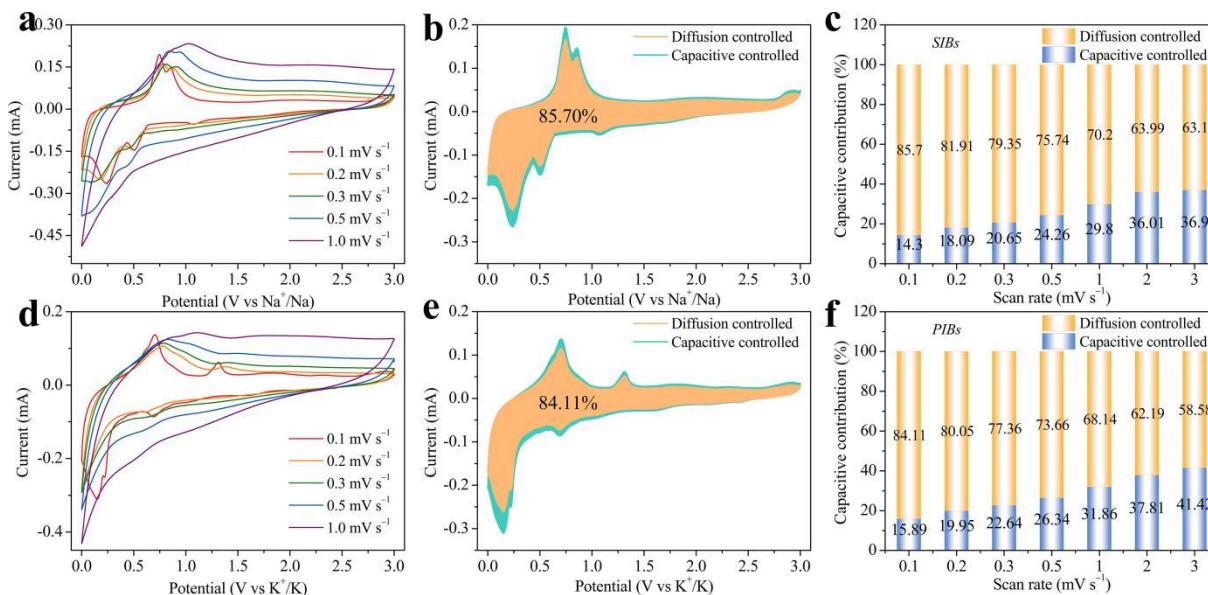

Figure 5. Electrochemical kinetics: (**a**) CV profiles at different scan rates, CV curves displaying capacity distribution (**b**) at 0.1 mV·s⁻¹ and (**c**) at various scan rates for SIBs; (**d**) CV profiles at different scan rates, CV curves displaying capacity distribution (**e**) at 0.1 mV·s⁻¹ and (**f**) at various scan rates for PIBs.

4. Conclusions

In summary, we propose THE Bi@rGO@NC architecture as anode material for Na- and K-ion storage. The robust hierarchical encapsulation engineering from graphene and N-doped C can effectively relieve the large lattice stress induced by huge volume variation, and is therefore conducive to the preservation of electrode integrity. Experimental characterization and theoretical calculation verify that the electron conductivity, Na-/-K-ion adsorption, and diffusion ability of Bi anode can be enhanced by double C to present great

electrochemical kinetic behavior. Therefore, outstanding alkaline-ion storage properties with a long-term lifespan of over 1000 cycles and superior rate capability can be achieved for Bi@rGO@NC electrode. This work provides an important reference for research into the Bi-based alloying composite anode material.

Supplementary Materials: The following supporting information can be downloaded at https://www.mdpi.com/article/10.3390/batteries9100505/s1. Figure S1: (a) XPS survey spectrum; (b) O 1s spectrum of Bi@rGO@NC. Figure S2: Ex situ FESEM images of Bi@rGO@NC after 20 cycles for (a) SIBs and (b) PIBs. Figure S3: Cycle performances of composite electrodes with and without N-doped C for SIBs at (a) 50 mA·g^{-1} and (b) 200 mA·g^{-1}. Figure S4: EIS plots of Bi@rGO@NC after 10 cycles.

Author Contributions: Investigation, formal analysis, and writing—original draft, S.Q.; conceptualization and supervision, Y.L.; methodology and writing—original draft, K.W.; conceptualization, methodology, supervision, writing—review and editing, S.C. All authors have read and agreed to the published version of the manuscript.

Data Availability Statement: Data will be made available on request.

Conflicts of Interest: The authors declare no conflict of interest.

References

1. Zhong, S.; Zhang, X.; Liu, J.; Sui, Y. Study on xLiVPO$_4$F·yLi$_3$V$_2$(PO$_4$)$_3$/C composite for high-performance cathode material for lithium-ion batteries. *Front. Chem.* **2020**, *8*, 361. [CrossRef] [PubMed]
2. Guo, X.; Guo, S.; Wu, C.; Li, J.; Liu, C.; Chen, W. Intelligent monitoring for safety-enhanced lithium-ion/sodium-ion batteries. *Adv. Energy Mater.* **2023**, *13*, 2203903. [CrossRef]
3. Lei, Y.J.; Liu, H.W.; Yang, Z.; Zhao, L.F.; Lai, W.H.; Chen, M.; Liu, H.; Dou, S.; Wang, Y.X. A review on the status and challenges of cathodes in room-temperature Na-S batteries. *Adv. Funct. Mater.* **2022**, *33*, 2212600. [CrossRef]
4. Chang, C.-B.; Lu, Y.-R.; Tuan, H.-Y. High-entropy NaCl-type metal chalcogenides as K-ion storage materials: Role of the cocktail effect. *Energy Storage Mater.* **2023**, *59*, 102770. [CrossRef]
5. Luo, P.; Zheng, C.; He, J.; Tu, X.; Sun, W.; Pan, H.; Zhou, Y.; Rui, X.; Zhang, B.; Huang, K. Structural engineering in graphite-based metal-ion batteries. *Adv. Funct. Mater.* **2021**, *32*, 2107277. [CrossRef]
6. Zhao, W.; Ma, X.; Yue, L.; Zhang, L.; Luo, Y.; Ren, Y.; Zhao, X.-E.; Li, N.; Tang, B.; Liu, Q.; et al. A gradient hexagonal-prism Fe$_3$Se$_4$@SiO$_2$@C configuration as a highly reversible sodium conversion anode. *J. Mater. Chem. A* **2022**, *10*, 4087–4099. [CrossRef]
7. Wu, X.; Leonard, D.P.; Ji, X. Emerging non-aqueous potassium-ion batteries: Challenges and opportunities. *Chem. Mater.* **2017**, *29*, 5031–5042. [CrossRef]
8. Zheng, J.; Yang, Y.; Fan, X.; Ji, G.; Ji, X.; Wang, H.; Hou, S.; Zachariah, M.R.; Wang, C. Extremely stable antimony-carbon composite anodes for potassium-ion batteries. *Energy Environ. Sci.* **2019**, *12*, 615–623. [CrossRef]
9. Chong, S.; Ma, M.; Yuan, L.; Qiao, S.; Dong, S.; Liu, H.; Dou, S. Hierarchical encapsulation and rich sp^{2}N assist Sb$_2$Se$_3$-based conversion-alloying anode for long-life sodium- and potassium-ion storage. *Energy Environ. Mater.* **2023**, *0*, e12458. [CrossRef]
10. Zhao, S.; Guo, Z.; Yan, K.; Guo, X.; Wan, S.; He, F.; Sun, B.; Wang, G. The rise of Prussian blue analogs: Challenges and opportunities for high-performance cathode materials in potassium-ion batteries. *Small Struct.* **2020**, *2*, 2000054. [CrossRef]
11. Zhang, X.; Yang, X.; Sun, G.; Yao, S.; Xie, Y.; Zhang, W.; Liu, C.; Wang, X.; Yang, R.; Jin, X.; et al. Hydration enables air-stable and high-performance layered cathode materials for both organic and aqueous potassium-ion batteries. *Adv. Funct. Mater.* **2022**, *32*, 2204318. [CrossRef]
12. Hong, Y.; Hu, J.; Tang, W.; Wei, B.; Guo, M.; Jia, S.; Fan, C. A universal small-molecule organic cathode for high-performance Li/Na/K-ion batteries. *Energy Storage Mater.* **2022**, *52*, 61–68. [CrossRef]
13. Li, H.; Xu, M.; Long, H.; Zheng, J.; Zhang, L.; Li, S.; Guan, C.; Lai, Y.; Zhang, Z. Stabilization of multicationic redox chemistry in polyanionic cathode by increasing entropy. *Adv. Sci.* **2022**, *9*, e2202082. [CrossRef] [PubMed]
14. Gao, X.; Liu, H.; Chen, H.; Mei, Y.; Wang, B.; Fang, L.; Chen, M.; Chen, J.; Gao, J.; Ni, L.; et al. Cationic-potential tuned biphasic layered cathodes for stable desodiation/sodiation. *Sci. Bull.* **2022**, *67*, 1589–1602. [CrossRef] [PubMed]
15. Zhang, J.; Kim, J.-B.; Zhang, J.; Lee, G.-H.; Chen, M.; Lau, V.W.-H.; Zhang, K.; Lee, S.; Chen, C.-L.; Jeon, T.-Y.; et al. Regulating pseudo-jahn-teller effect and superstructure in layered cathode materials for reversible alkali-ion intercalation. *J. Am. Chem. Soc.* **2022**, *144*, 7929–7938. [CrossRef] [PubMed]

16. Sha, M.; Liu, L.; Zhao, H.; Lei, Y. Review on recent advances of cathode materials for potassium-ion batteries. *Energy Environ. Mater.* **2020**, *3*, 56–66. [CrossRef]

17. Peng, B.; Wan, G.; Ahmad, N.; Yu, L.; Ma, X.; Zhang, G. Recent progress in the emerging modification strategies for layered oxide cathodes toward practicable sodium ion batteries. *Adv. Energy Mater.* **2023**, *13*, 202300334. [CrossRef]

18. Liu, X.; Cao, Y.; Sun, J. Defect engineering in Prussian blue analogs for high-performance sodium-ion batteries. *Adv. Energy Mater.* **2022**, *12*, 2202532. [CrossRef]

19. Li, C.; Wang, S. Improving strategies for the molecular structure of organic anode/cathode materials in potassium-ion batteries. *EcoMat* **2022**, *4*, e12246. [CrossRef]

20. Lei, H.; Li, J.; Zhang, X.; Ma, L.; Ji, Z.; Wang, Z.; Pan, L.; Tan, S.; Mai, W. A review of hard carbon anode: Rational design and advanced characterization in potassium ion batteries. *InfoMat* **2022**, *4*, e12272. [CrossRef]

21. Hu, J.; Hong, Y.; Guo, M.; Hu, Y.; Tang, W.; Xu, S.; Jia, S.; Wei, B.; Liu, S.; Fan, C.; et al. Emerging organic electrodes for Na-ion and K-ion batteries. *Energy Storage Mater.* **2023**, *56*, 267–299. [CrossRef]

22. Soltani, N.; Bahrami, A.; Giebeler, L.; Gemming, T.; Mikhailova, D. Progress and challenges in using sustainable carbon anodes in rechargeable metal-ion batteries. *Prog. Energy Combust.* **2021**, *87*, 100929. [CrossRef]

23. Wang, X.; Tang, S.; Guo, W.; Fu, Y.; Manthiram, A. Advances in multimetallic alloy-based anodes for alkali-ion and alkali-metal batteries. *Mater. Today* **2021**, *50*, 259–275. [CrossRef]

24. Lv, Z.; Xu, H.; Xu, W.; Peng, B.; Zhao, C.; Xie, M.; Lv, X.; Gao, Y.; Hu, K.; Fang, Y.; et al. Quasi-topological intercalation mechanism of $Bi_{0.67}NbS_2$ enabling 100 C fast-charging for sodium-ion batteries. *Adv. Energy Mater.* **2023**, *13*, 2300790. [CrossRef]

25. Liu, X.; Zhu, J.; Wang, X.; Yue, L.; Wang, W.; Wang, B.; Shen, D.; Li, Y. Boosting potassium storage kinetics, stability, and volumetric performance of honeycomb-like porous red phosphorus via in situ embedding self-growing conductive nano-metal networks. *Adv. Funct. Mater.* **2022**, *33*, 2209388. [CrossRef]

26. Xiong, P.; Bai, P.; Li, A.; Li, B.; Cheng, M.; Chen, Y.; Huang, S.; Jiang, Q.; Bu, X.H.; Xu, Y. Bismuth nanoparticle@carbon composite anodes for ultralong cycle life and high-rate sodium-ion batteries. *Adv. Mater.* **2019**, *31*, e1904771. [CrossRef] [PubMed]

27. Sun, Z.; Liu, Y.; Ye, W.; Zhang, J.; Wang, Y.; Lin, Y.; Hou, L.; Wang, M.S.; Yuan, C. Unveiling intrinsic potassium storage behaviors of hierarchical nano Bi@N-doped carbon nanocages framework via in situ characterizations. *Angew. Chem. Int. Ed.* **2021**, *60*, 7180–7187. [CrossRef] [PubMed]

28. Hirahara, T.; Nagao, T.; Matsuda, I.; Bihlmayer, G.; Chulkov, E.V.; Koroteev, Y.M.; Hasegawa, S. Quantum well states in ultrathin Bi films: Angle-resolved photoemission spectroscopy and first-principles calculations study. *Phys. Rev. B* **2007**, *75*, 035422. [CrossRef]

29. Liang, Y.; Song, N.; Zhang, Z.; Chen, W.; Feng, J.; Xi, B.; Xiong, S. Integrating Bi@C nanospheres in porous hard carbon frameworks for ultrafast sodium storage. *Adv. Mater.* **2022**, *34*, e2202673. [CrossRef]

30. Yang, H.; Chen, L.W.; He, F.; Zhang, J.; Feng, Y.; Zhao, L.; Wang, B.; He, L.; Zhang, Q.; Yu, Y. Optimizing the void size of yolk-shell Bi@void@C nanospheres for high-power-density sodium-ion batteries. *Nano Lett.* **2020**, *20*, 758–767. [CrossRef]

31. Zhang, F.; Liu, X.; Wang, B.; Wang, G.; Wang, H. Bi@C nanospheres with the unique petaloid core-shell structure anchored on porous graphene nanosheets as an anode for stable sodium- and potassium-ion batteries. *ACS Appl. Mater. Interfaces* **2021**, *13*, 59867–59881. [CrossRef] [PubMed]

32. Qiao, S.; Zhou, Q.; Ma, M.; Liu, H.K.; Dou, S.X.; Chong, S. Advanced anode materials for rechargeable sodium-ion batteries. *ACS Nano* **2023**, *17*, 11220–11252. [CrossRef] [PubMed]

33. Ma, M.; Chong, S.; Yao, K.; Liu, H.K.; Dou, S.X.; Huang, W. Advanced anode materials for potassium batteries: Sorting out opportunities and challenges by potassium storage mechanisms. *Matter* **2023**, *6*, 1–54. [CrossRef]

34. Chen, M.; Zhou, L.; Wang, T.; Xia, H.; Liu, H.K.; Dou, S.X.; Chou, S. Nitrogen as an anionic center/dopant for next-generation high-performance lithium/sodium-ion battery electrodes: Key scientific issues, challenges and perspectives. *Adv. Funct. Mater.* **2023**, *33*, 2214786. [CrossRef]

35. Su, D.; Dou, S.; Wang, G. Bismuth: A new anode for the Na-ion battery. *Nano Energy* **2015**, *12*, 88–95. [CrossRef]

36. Zhang, Q.; Mao, J.; Pang, W.K.; Zheng, T.; Sencadas, V.; Chen, Y.; Liu, Y.; Guo, Z. Boosting the potassium storage performance of alloy-based anode materials via electrolyte salt chemistry. *Adv. Energy Mater.* **2018**, *8*, 1703288. [CrossRef]

37. Cai, S.; Yan, F.; Zhao, Y.; Li, M.; Chen, Y.; He, X.; Wang, C. Hierarchical micro-composite assembled from Bi spheres and expanded graphite flakes as anodes for sodium-ion half/full cells with excellent comprehensive electrochemical performance. *Chem. Eng. J.* **2022**, *430*, 132938. [CrossRef]

38. Wang, A.; Hong, W.; Yang, L.; Tian, Y.; Qiu, X.; Zou, G.; Hou, H.; Ji, X. Bi-based electrode materials for alkali metal-ion batteries. *Small* **2020**, *16*, 2004022. [CrossRef]

39. Ngaloy, R.T.; Fontanilla, A.M.; Soriano, M.S.R.; Pascua, C.S.; Matsushita, Y.; Agulo, I.J.A. Highly efficient photocatalysis by zinc oxide-reduced graphene oxide (ZnO-rGO) composite synthesized via one-pot room-temperature chemical deposition method. *J. Nanotechnol.* **2019**, *2019*, 1895043. [CrossRef]

40. Hong, W.; Wang, A.; Li, L.; Qiu, T.; Li, J.; Jiang, Y.; Zou, G.; Peng, H.; Hou, H.; Ji, X. Bi dots confined by functional carbon as high-performance anode for lithium ion batteries. *Adv. Funct. Mater.* **2020**, *31*, 2000756. [CrossRef]

41. Cen, Y.; Dong, J.; Zhu, T.; Cai, X.; Wang, X.; Hu, B.; Xu, C.; Yu, D.; Liu, Y.; Chen, C. Bi nanorods anchored in N-doped carbon shell as anode for high-performance magnesium ion batteries. *Electrochim. Acta* **2021**, *397*, 139260. [CrossRef]

42. Cheng, M.; Liu, J.; Wang, X.; Li, Y.; Xia, W.; Liu, Q.; Hu, J.; Wei, T.; Ling, Y.; Liu, B.; et al. In-situ synthesis of Bi nanospheres anchored in 3D interconnected cellulose nanocrystal derived carbon aerogel as anode for high-performance Mg-ion batteries. *Chem. Eng. J.* **2023**, *451*, 138824. [CrossRef]

43. Chong, S.; Qiao, S.; Wei, X.; Li, T.; Yuan, L.; Dong, S.; Huang, W. Sb₂S₃-based conversion-alloying dual mechanism anode for potassium-ion batteries. *iScience* **2021**, *24*, 103494. [CrossRef] [PubMed]

44. Topçu, E.; Dağcı Kıranşan, K. Flexible gold nanoparticles/rGO and thin film/rGO papers: Novel electrocatalysts for hydrogen evolution reaction. *J. Chem. Technol. Biotechnol.* **2019**, *94*, 3895–3904. [CrossRef]

45. Wang, Y.; Zhou, Y.; Shen, Y.; Zhu, S. Pyridinic N: A special group for enhancing direct decomposition reaction of NO over N-doped porous carbon. *Micropor. Mesopor. Mat.* **2018**, *265*, 98–103. [CrossRef]

46. Pan, Y.; Cheng, X.; Gao, M.; Fu, Y.; Feng, J.; Gong, L.; Ahmed, H.; Zhang, H.; Battaglia, V.S. Cagelike CoSe₂@N-doped carbon aerogels with pseudocapacitive properties as advanced materials for sodium-ion batteries with excellent rate performance and cyclic stability. *ACS Appl. Mater. Interfaces* **2020**, *12*, 33621–33630. [CrossRef] [PubMed]

47. Xue, P.; Wang, N.; Fang, Z.; Lu, Z.; Xu, X.; Wang, L.; Du, Y.; Ren, X.; Bai, Z.; Dou, S.; et al. Rayleigh-instability-induced bismuth nanorod@nitrogen-doped carbon nanotubes as a long cycling and high rate anode for sodium-ion batteries. *Nano Lett.* **2019**, *19*, 1998–2004. [CrossRef] [PubMed]

48. Kowalczyk, P.J.; Mahapatra, O.; Mccarthy, D.N.; Kozlowski, W.; Klusek, Z.; Brown, S.A. STM and XPS investigations of bismuth islands on HOPG. *Surf. Sci.* **2011**, *605*, 659–667. [CrossRef]

49. Liu, H.; He, Y.; Cao, K.; Wang, S.; Jiang, Y.; Liu, X.; Huang, K.J.; Jing, Q.S.; Jiao, L. Potassium-ion batteries: Stimulating the reversibility of Sb₂S₃ anode for high-performance potassium-ion batteries. *Small* **2021**, *17*, 2170044. [CrossRef]

50. Zhou, Q.; Yuan, L.; Li, T.; Qiao, S.; Ma, M.; Wang, Y.; Chong, S. Boosting cobalt ditelluride quantum-rods anode materials for excellent potassium-ion storage via hierarchical physicochemical encapsulation. *J. Colloid. Interface Sci.* **2023**, *646*, 493–502. [CrossRef]